



Open Research Online

Citation

Martínez-Alvarado, Oscar; Moroz, Irene M.; Read, Peter L.; Lewis, Stephen R. and Montabone, Luca (2009). Low-order dynamical behavior in the martian atmosphere: Diagnosis of general circulation model results. *Icarus*, 204(1) pp. 48–62.

URL

<https://oro.open.ac.uk/17944/>

License

None Specified

Policy

This document has been downloaded from Open Research Online, The Open University's repository of research publications. This version is being made available in accordance with Open Research Online policies available from [Open Research Online \(ORO\) Policies](#)

Versions

If this document is identified as the Author Accepted Manuscript it is the version after peer review but before type setting, copy editing or publisher branding

Accepted Manuscript

Low-order dynamical behaviour in the Martian atmosphere: Diagnosis of general circulation model results

Oscar Martínez-Alvarado, Irene M. Moroz, Peter L. Read, Stephen R. Lewis, Luca Montabone

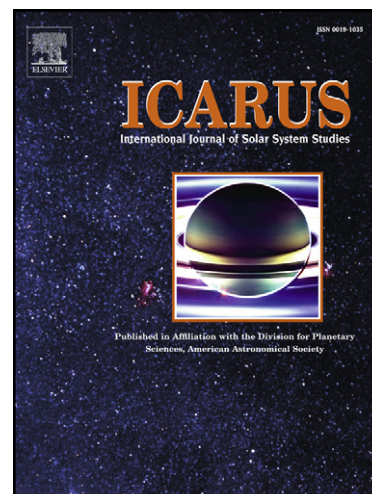
PII: S0019-1035(09)00252-8
DOI: [10.1016/j.icarus.2009.06.010](https://doi.org/10.1016/j.icarus.2009.06.010)
Reference: YICAR 9072

To appear in: *Icarus*

Received Date: 27 August 2008
Revised Date: 14 May 2009
Accepted Date: 7 June 2009

Please cite this article as: Martínez-Alvarado, O., Moroz, I.M., Read, P.L., Lewis, S.R., Montabone, L., Low-order dynamical behaviour in the Martian atmosphere: Diagnosis of general circulation model results, *Icarus* (2009), doi: [10.1016/j.icarus.2009.06.010](https://doi.org/10.1016/j.icarus.2009.06.010)

This is a PDF file of an unedited manuscript that has been accepted for publication. As a service to our customers we are providing this early version of the manuscript. The manuscript will undergo copyediting, typesetting, and review of the resulting proof before it is published in its final form. Please note that during the production process errors may be discovered which could affect the content, and all legal disclaimers that apply to the journal pertain.



Low-order dynamical behaviour in the Martian atmosphere: Diagnosis of general circulation model results

OSCAR MARTÍNEZ-ALVARADO

E: O.MartinezAlvarado@reading.ac.uk, T: +44 (0)118 378 7995, F: +44 (0)118 378 8905

MATHEMATICAL INSTITUTE, UNIVERSITY OF OXFORD

24-29 ST GILES, OXFORD, OX1 3LB, UK

NOW AT: DEPARTMENT OF METEOROLOGY, UNIVERSITY OF READING

EARLEY GATE, PO BOX 243, READING, RG6 6BB, UK

IRENE M. MOROZ

E: moroz@maths.ox.ac.uk, T: +44 (0)1865 270514, F: +44 (0)1865 273583

MATHEMATICAL INSTITUTE, UNIVERSITY OF OXFORD

24-29 ST GILES, OXFORD, OX1 3LB, UK

PETER L. READ

E: p.read1@physics.ox.ac.uk, T: +44 (0)1865 272082, F: +44 (0)1865 272923

CLARENDON LABORATORY, UNIVERSITY OF OXFORD

PARKS ROAD, OXFORD, OX1 3PU, UK

STEPHEN R. LEWIS

E: S.R.Lewis@open.ac.uk, T: +44 (0)1908 655803, F: +44 (0)1908 654192

LUCA MONTABONE

E: montabone@atm.ox.ac.uk, T: +44 (0)1865 272902, F: +44 (0)1865 272923

DEPARTMENT OF PHYSICS AND ASTRONOMY, THE OPEN UNIVERSITY

WALTON HALL, MILTON KEYNES, MK7 6AA, UK

June 22, 2009

67 pages, 19 figures, 3 tables

Proposed running head:

Low-order dynamics in the Martian atmosphere

Corresponding author:

Oscar Martínez-Alvarado

Current address:

Department of Meteorology

University of Reading

Earley Gate, PO Box 243

Reading, RG6 6BB

United Kingdom

E-mail: O.MartinezAlvarado@reading.ac.uk

Telephone: +44 (0)118 378 7995

Fax: +44 (0)118 378 8905

Abstract

The hypothesis of a low dimensional Martian climate attractor is investigated by the application of the proper orthogonal decomposition (POD) to a simulation of Martian atmospheric circulation using the UK Mars general circulation model (UK-MGCM). In this article we focus on a time series of the interval between autumn and winter in the northern hemisphere, when baroclinic activity is intense. The POD is a statistical technique that allows the attribution of total energy (TE) to particular structures embedded in the UK-MGCM time-evolving circulation. These structures are called empirical orthogonal functions (EOFs). Ordering the EOFs according to their associated energy content, we were able to determine the necessary number to account for a chosen amount of atmospheric TE. We shown that for Mars a large fraction of TE is explained by just a few EOFs (with 90% TE in 23 EOFs), which apparently support the initial hypothesis. We also show that the resulting EOFs represent classical types of atmospheric motion, such as thermal tides and transient waves. Thus, POD is shown to be an efficient method for the identification of different classes of atmospheric modes. It also provides insight into the nonlinear interaction of these modes.

Keywords: Mars; atmospheres, dynamics; data reduction techniques.

1 Introduction

A number of observational studies and numerical simulations have suggested that the dynamical behaviour of the Martian atmosphere may be more regular and coherent than its terrestrial counterpart. For example, the analysis of meteorological information sent back to the Earth by Viking Lander 2 during two consecutive Martian years showed that transient baroclinic wave activity in the northern hemisphere was characterized by rather similar parameters, suggesting similar dynamics, during spring and autumn in both years (Barnes, 1980, Barnes, 1981). This regularity in the behaviour of transient waves was also found in simulations carried out using the NASA Ames General Circulation Model (GCM) (Barnes *et al.*, 1993).

An early series of numerical experiments with the UK Mars GCM (UK-MGCM) suggested that, without the influence of the diurnal cycle, the Martian atmosphere would display a behaviour characterized by coherent baroclinic waves during late autumn, winter and early spring with periods of approximately 2.2 or 5.5 sols (1 sol = 1 Martian solar day). When the diurnal cycle was included, the baroclinic waves no longer displayed a regular behaviour. Instead, they evolved in a more irregular way which was, nevertheless, influenced to a large extent by episodic oscillations with periods of 2.6 and 5.6 sols (Collins *et al.*, 1996). Both numerical experiments produced the same zonal structure for the baroclinic waves. Thus, the high-frequency baroclinic waves displayed a horizontal structure with zonal wavenumber two in both simulations while the low-frequency waves had a zonal wavenumber-1 wave structure (Collins *et al.*, 1996). In this manner thermal tides and

baroclinic waves appear to be spatially resonant, which would suggest that complex non-linear interactions between these different kind of motions are to be expected (Collins *et al.*, 1996). In fact these results can be interpreted as a complex dynamical pattern controlled by two coexisting equilibria. The system would tend to stay near one of the equilibria until it was perturbed by the diurnal cycle which would then cause the system to switch erratically from one equilibrium state to another (Read and Lewis, 2004).

These findings constitute rather intriguing features of the Martian atmosphere considering the high complexity that would be expected in such a system. The enhanced regularity observed in the dynamical behaviour of the atmosphere of Mars in comparison with its terrestrial counterpart suggests the hypothesis of a relatively low-dimensional underlying attractor of the Martian climate. In turn, this hypothesis points towards the possibility of analysing the Martian atmosphere in the context of low-order diagnostic and, in principle, prognostic models.

Low-order models based on proper orthogonal decomposition (POD) have been under development for the terrestrial case for some time (e.g. Schubert, 1985). However, work on low-dimensional models in the context of planetary atmospheres is still sparse despite the potential significance that this kind of research could have for the study of extraterrestrial atmospheres and comparative planetology.

One example of these studies is given by the work of Whitehouse *et al.* (2005a, 2005b). They analyzed the possibility of representing an atmospheric dataset by a small number of modes (Whitehouse *et al.*, 2005a). Their atmospheric dataset was produced by a simplified GCM (SGCM) for a planet

with no topography (smooth surface with no variation in thermal properties) and simple physical parametrizations such as Newtonian cooling and Rayleigh friction. The parameters in the model were tuned as for resembling the behaviour of the atmosphere of Mars as described by Collins and James (1995). Whitehouse *et al.* (2005a) carried out a two-stage decomposition on the quasi-geostrophic (QG) horizontal streamfunction. First, they decomposed this field in a series of vertical modes based on the QG vertical structure equation. After this first decomposition, they compiled a partially reduced dataset by choosing those vertical modes that explained most of the energy content in the original dataset. The reduced dataset was subject to further reduction by means of POD, a statistical technique for extracting coherent structures from experimental or simulated data according to a suitably defined generalized energy (see Holmes *et al.*, 1996, and Section 3.1 below for a more complete description of POD). The complete procedure allowed the representation of $\mathcal{O}(10^3)$ ensemble members by a set of $\mathcal{O}(50)$ EOFs. Dynamically, this effectively amounts to the reduction from $\mathcal{O}(10^4)$ degrees of freedom in the original model down to $\mathcal{O}(50)$ degrees of freedom in the fully reduced dataset (Whitehouse *et al.* (2005a).

In a second article, Whitehouse *et al.* (2005b) introduced the construction of dynamical reduced-dimension models for the SGCM based on the decomposition described above. They managed to construct successful models with 80 degrees of freedom in a combination of vertical and horizontal modes derived during the diagnostic analysis previously described.

Closely following the programme established by Whitehouse *et al.* (2005a, 2005b), this and a forthcoming article explore the hypothesis of a relatively

low-dimensional attractor underlying the Martian climate by searching for low-order models capable of representing the essential dynamics of the Martian atmosphere. In particular, this article presents a diagnostic analysis of simulated data by the UK-MGCM. In contrast with the idealized SGCM used by Whitehouse *et al.* (2005a, 2005b), the UK-MGCM is a state-of-the-art model comprising complex parametrizations for a number of relevant physical processes such as radiative heat transfer, surface processes, sub-grid dynamics and polar carbon dioxide condensation and sublimation. It also includes a realistic representation of the Martian topography as measured by the Mars Orbiter Laser Altimeter (MOLA) aboard the Mars Global Surveyor (MGS) spacecraft (Smith *et al.*, 1999).

The approach of the present study is focused on the use of the primitive equations of dynamic meteorology as underlying dynamics rather than the QG theory approach of previous studies (Whitehouse *et al.*, 2005a, 2005b). This choice positions our study close to the latest work in the terrestrial context (Achatz and Opsteegh, 2003). The UK-MGCM and the climatology of the UK-MGCM simulation to be analyzed will be described in Section 2. As a consequence of this approach, the analysis was carried out by means of a fully three dimensional version of POD, which involved the simultaneous decomposition of the horizontal components of velocity, temperature and surface pressure. Horizontal velocity components and temperature were functions of three spatial dimensions (planetographic longitude and latitude, and sigma as a vertical coordinate) while surface pressure was a function only of longitude and latitude. The four fields were time dependent. The full description of this method is given in Section 3.1. In Section 4, the en-

ergy distribution as extracted by POD is presented. Section 5 investigates the relation between POD-modes, or empirical orthogonal functions (EOFs), and components of atmospheric motions such as thermal tides and baroclinic waves, that have been the subject of extensive studies. By establishing this relationship we seek to shed light on the appropriate physical interpretation of the EOFs for this problem. Furthermore, we intend to show that thermal tides and transient waves are intimately related not only by sharing similar energy contents but also by being part of common coherent structures, which confirms and extend the findings by Collins *et al.* (1996). Finally, a summary and conclusions are given in Section 6.

2 The UK Mars GCM

The UK-MGCM is a pseudo-spectral model jointly developed at the University of Oxford and the Open University in collaboration with the Laboratoire de Météorologie Dynamique (LMD) in Paris. It is based on the terrestrial model of Hoskins and Simmons (1975). The resolution used in the simulation for this study was jagged T31 (triangular with maximum total wavenumber 31) with 25 unevenly-spaced σ -levels in the vertical. The uneven spacing in the vertical allows for an enhanced resolution near the surface (Forget *et al.*, 1999). The uppermost full level is located at $\sigma = 5.6 \times 10^{-5}$, approximately corresponding to 100 km assuming a constant scale height $H = 10$ km. This vertical extension allows the model to capture the fully developed Martian Hadley cell, which can reach heights of around 80 km (Wilson, 1997).

The large-scale topographic features on Mars play an essential role in the

evolution of the general circulation. For example, coupled with the diurnal tide, it is well-known to excite waves that resemble non-migrating tides (Zurek, 1976). In particular, an eastward-propagating diurnal Kelvin wave and a westward-propagating wavenumber-3 diurnal wave arise from this interaction. The diurnal Kelvin wave seems to have an influence on processes such as the development of dust storms (Montabone *et al.*, 2007). Therefore, it is important to have an accurate representation of Mars' topography. The UK-MGCM uses the highly accurate Mars topography dataset as measured by the Mars Orbiter Laser Altimeter (MOLA) aboard NASA's Mars Global Surveyor spacecraft (MGS) (Smith *et al.*, 1999).

The physical processes in the model include radiative heat transfer, surface processes, sub-grid dynamics and carbon dioxide mass exchange between the polar caps and the atmosphere (Forget *et al.*, 1999; Read and Lewis, 2004, and references therein). The latter is largely responsible for the significant surface pressure variations along the Martian year.

2.1 UK-MGCM dataset climatology

In order to reduce the amount of information to be handled by POD, thereby reducing the computational expense, only 10 unevenly spaced sigma-levels were selected from the sigma-levels in the UK-MGCM. Table 1 shows the sigma-levels in the UK-MGCM. The levels that were retained are enclosed in a box. The lower levels were chosen so that the first scale height ($H_0 = 10$ km, on Mars) was well represented. Thus, the first four levels lay within the first 10 km and the fifth is just above. The uppermost levels in the UK-

MGCM were discarded to avoid including the sponge layer. The horizontal resolution was set to a regular longitude-latitude grid with $I = 64$ grid points in the zonal direction and $J = 32$ grid points in the meridional direction for vorticity, potential vorticity and streamfunction.

The UK-MGCM data was transformed into time series of zonal and latitudinal velocity and temperature on the 10 sigma-levels used for POD plus pressure at the surface. Each level was discretized in a 64×32 regular longitude-latitude grid, corresponding to squares of angular length 5.625° in either direction and equivalent to a maximum arc length of $s = 333$ km. The variables were distributed over a C-grid (Arakawa and Lamb, 1977).

The UK-MGCM dataset that was used in this study covers a 90-sol interval from $L_s = 267.7^\circ$ (sol 511) to $L_s = 323.2^\circ$ (sol 601). Here L_s is the areocentric longitude and gives the position of the planet in its orbit around the sun. $L_s = 0, 90, 180, 270^\circ$ correspond to the northern spring equinox, summer solstice, autumn equinox and winter solstice, respectively. Thus, this dataset corresponds to the transition between autumn and winter in the northern hemisphere. The simulation was carried out with a dust scenario which prescribes the total dust optical depth at each latitude and time of the year. This scenario (MGS dust scenario) has been derived from MGS observations and produces temperature profiles in the model which are close to those observed by the Thermal Emission Spectrometer aboard MGS (Smith *et al.*, 2001). The time series was sampled every two hours to make an ensemble of 1080 elements.

2.1.1 Zonal mean

Figure 1 shows the temporal and zonal average of temperature and zonal wind in the UK-MGCM for the period under consideration. Figure 1 also shows the meridional mass transport streamfunction χ defined, in sigma-coordinates, as (e.g., Gill, 1982)

$$\overline{p_s v} = -\frac{1}{\cos \phi} \frac{\partial \chi}{\partial \sigma}, \quad \overline{p_s \sigma} = \frac{1}{\cos \phi} \frac{\partial \chi}{\partial \phi}, \quad (1)$$

where $\overline{(\cdot)}$ indicates zonal average so that positive streamfunction indicates counter-clockwise circulation.

Figure 1 presents a zonal mean atmospheric structure with characteristics typical of winter solstice. A steep horizontal temperature gradient near the surface in the winter hemisphere gives rise to a very strong winter westerly jet in the middle atmosphere above the northern hemisphere, reaching peak speeds of 140 m s^{-1} on average. This jet is accompanied by a weaker easterly jet above the equator. The temperature cross-section (Fig. 1) exhibits the so-called winter polar warming that takes place in the middle atmosphere between 50 and 80 km (Read and Lewis, 2004). This phenomenon is due to adiabatic compression in the downwards side of the Hadley cell, which on Mars extends up to 80 km above the surface (Wilson, 1997, Forget *et al.*, 1999). Notice also the strong hemispheric asymmetry of the Martian solstice general circulation. This is characterized by a strong quasi-global Hadley cell that extends from almost 60° in the summer hemisphere to the pole in the opposite hemisphere (Forget *et al.*, 1999).

2.1.2 Atmospheric tides

There are two important features of the UK-MGCM which have an impact on the global circulation: the presence of diurnal and seasonal cycles and the inclusion of topography. These three features are relevant for this study. However, the effect of the seasonal cycle will only be partially included due to the short duration of the time series under analysis. Therefore, we will focus our analysis on the effects of the diurnal cycle.

The presence of the diurnal cycle gives rise to atmospheric thermal tides. These are atmospheric motions whose characteristic periods are harmonics of 1 sol. They can be classified as sun-synchronous, or migrating, and longitude-dependent, or non-migrating, tides. The most significant migrating tides are the diurnal and semidiurnal tides (see, e.g. Wilson and Hamilton, 1996).

The diurnal tide is a westward-travelling wave, characterized by a zonal wavenumber one and a period of 1 sol. The semidiurnal tide is also a westward-travelling wave, though it is characterized by a zonal wavenumber two and a period of half a sol. The diurnal tide is mainly the response of the atmosphere to surface heating because of its short vertical wavelength and surface-trapped structure. The semidiurnal tide, on the other hand, has a much longer vertical wavelength and reflects the vertically integrated radiative response of the atmosphere. Hence, the activity of the semidiurnal tide has a central influence on the atmospheric response to radiatively active phenomena such as dust storms, when the vertical radiative properties are changed due to the enhanced presence of dust loadings (Lewis and Barker, 2005).

On Mars an eastward-propagating diurnal Kelvin wave characterized by a zonal wavenumber one and a resonant period close to 1 sol (e.g., Zurek, 1976, Forbes, 2004, Lewis and Barker, 2005) plays the role of a non-migrating tide. It arises from the interaction between the diurnal tide and topography dominated by a strong zonal wavenumber-2 pattern (Zurek, 1976). Hence, it can only be simulated in a model which includes appropriate topographic information (Forbes, 2004, Read and Lewis, 2004). The interaction between the diurnal tide and topography also gives rise to a westward propagating wavenumber-3 wave with a period of 1 sol.

Figure 2 is a graphical representation on a period-wavenumber space of atmospheric planetary waves present on average in the UK-MGCM dataset as seen in two different fields (a negative period represents a wave travelling westwards). Figure 2(a) corresponds to surface pressure (cf. Fig. 5.9 in Read and Lewis, 2004); Fig. 2(b) presents the same information as seen in the temperature at an approximate height of 600 m above the planetary surface. These figures were obtained by a double Fourier transform (in time and longitude) of a surface pressure (or temperature) time series around the equator (Read and Lewis, 2004, Lewis and Barker, 2005). For the Fourier transform in time we used a rectangular window of 20 sols in order to get a sufficient resolution in frequency. The window was slid along the time axis in steps of 2 Martian hours. The resulting time series of spectral coefficients was then averaged in time.

The strongest signal in both fields corresponds to the westward-propagating diurnal tide (Period = -1 sol, $m = 1$). The semidiurnal tide (Period = -0.5 sol, $m = 2$) and the diurnal Kelvin wave (Period = +1 sol, $m = 1$) are present

in both fields as well as the westward propagating diurnal wavenumber-3 wave (Period = -1 sol, $m = 3$). However, these waves have different impact on each field. In the surface pressure signal, the diurnal Kelvin wave is the second strongest, followed by the semidiurnal tide. In contrast, in the temperature field at the level of observation, the semidiurnal mode is the second most significant followed by the westward propagating diurnal wavenumber-3 wave.

A similar analysis at mid-latitudes in the northern hemisphere reveals a completely different atmospheric structure at mid-latitudes. Figure 3(a) shows a frequency-wavenumber diagram for atmospheric planetary waves in surface pressure on a longitudinal circle at 64.3°N ; Fig. 3(b) presents similar information for temperature at an approximate height of 600 m above the planetary surface on the same longitudinal circle. At this level the most important signal comes from slow eastward-moving waves with periods ranging from approximately 1.8 to 5.5 sols and zonal wavenumbers between 1 and 3. These waves correspond to baroclinic activity taking place at mid-latitudes in the northern hemisphere similar to that found in previous studies using this same MGCM (Collins *et al.*, 1996). These waves represent the model's response to baroclinic instability. They are related to the baroclinic activity first detected in the analysis of Viking 1 and 2 surface pressure data (Barnes, 1980; Barnes, 1981). However, the wavenumbers predicted by the UK-MGCM are somewhat different from those envisaged by Barnes (1980). This is an important difference between the model and the actual planet which should be born in mind during this analysis.

Figure 3

As on the equator, an indication of vertical structure can be deduced from the dissimilarities in the waves at the surface and at slightly higher

levels in the atmosphere. For example, the maximum power contribution to the surface pressure comes from zonal wavenumber-1 waves, whereas zonal wavenumber-2 waves contribute the most to the power observed in temperature at 600 m above the surface. Furthermore, the diurnal tide is still perceptible at the surface whereas its signal has vanished when observed at an altitude of only 600 m above the surface. This effect is due to the presence of the seasonal CO₂ polar cap, which effectively locks temperature values to the CO₂ frost point. Indeed, looking at higher altitudes, the strength of the tides is recovered in a picture similar to Fig. 3(a).

An important difference (not captured by the figures) between the dynamics at the equator and at mid-latitudes is that there was a constant change in the power of waves at different frequencies and zonal wavenumbers at mid-latitudes for the time interval under analysis. In contrast, the power distribution at the equator did not vary considerably and the picture remained pretty much the same as that shown in Fig. 2.

3 Analysis methodology

The analysis methodology that was used in this work consisted of a combination of proper orthogonal decomposition (POD) and short-time Fourier analysis. This combination allows us to identify the distribution of the energy (via POD) and relate this to the tidal modes and natural modes that occur in the atmosphere (via Fourier analysis). In this section we review these two methods and explain the way in which we have combined them in order to achieve our objective.

3.1 Proper orthogonal decomposition

Proper orthogonal decomposition is a statistical technique that originally was intended as a compression tool to represent most of the variance in a given dataset using the smallest number of modes (Karhunen, 1946, Loève, 1945). Then, it was found to be useful in the study of turbulence in fluids (Lumley, 1970) and more recently as a tool, in combination with Galerkin projection techniques, to construct low-order dynamical models of very high-dimensional systems whose attractors are believed to be restricted to a lower dimensional space (Holmes *et al.*, 1996). The systems to which the technique has been applied range from fluid turbulence (e.g., Smith *et al.*, 2005) and atmospheric physics (e.g., Achatz and Opsteegh, 2003) to control theory (e.g., Rowley *et al.*, 2001). The resulting POD-Galerkin models have been proved to be successful in at least some cases at capturing the most important features of specific systems using a limited number of POD modes, sometimes called empirical orthogonal functions (EOFs). This article is focused on the analysis of an atmospheric dataset derived from simulations with the UK-MGCM. In a forthcoming paper we will combine the results presented here with the Galerkin projection of the primitive equations to construct low-order dynamical models.

POD can be set to optimize either variance or other forms of generalized energy depending on the definition of a norm to measure the space of states. The correlation or kinetic-energy (KE) norm (used in statistical analysis of data and incompressible homogeneous fluid studies) is one example. Another one, incorporating greater generality, is the total-energy (TE) norm. The

description of a stratified and/or compressible fluid requires not only the velocity components but also one or more thermodynamic variables. This is an example where the TE norm is useful since it allows the incorporation of variables of different kinds in its definition. Atmospheric models constitute a second example where the TE norm has been found to be an appropriate choice (Achatz and Opsteegh, 2003, Whitehouse *et al.*, 2005a). In agreement with this findings, we use atmospheric TE as a norm in this study.

Assuming hydrostatic balance, atmospheric TE for an air column is given by

$$e = \int_{z_0}^{\infty} \rho \left(\frac{1}{2} \mathbf{v} \cdot \mathbf{v} + c_v T + gz \right) dz, \quad (2)$$

where ρ is density, \mathbf{v} is horizontal velocity, T is temperature, z is height and z_0 is topographic height. Also, $c_v = 629 \text{ J kg}^{-1} \text{ K}^{-1}$ is the heat capacity at constant volume and $g = 3.72 \text{ m s}^{-2}$ is the acceleration due to gravity. The first term in the integrand of Eq. 2 represents kinetic energy, while the second term represents internal energy and the third one represents gravitational potential energy. It can be shown that the last two terms can be written as atmospheric total potential energy (TPE) plus a surface term (e.g. Houghton, 2002)

$$\int_{z_0}^{\infty} \rho (c_v T + gz) dz = \int_0^{p_s} \frac{c_p}{g} T dp + \frac{1}{g} \Phi_s p_s, \quad (3)$$

where $c_p = 820 \text{ J kg}^{-1} \text{ K}^{-1}$ is the heat capacity at constant pressure, p is local pressure, Φ_s is geopotential height at the surface (topography), and p_s is surface pressure.

Since we want to express TE as a norm it is necessary to write it as a quadratic form of the state variables. This can be achieved by first non-

dimensionalizing our equations. For this purpose, the planetary radius a and the reciprocal rotation rate Ω^{-1} ($a = 3.3960 \times 10^6$ m, $\Omega = 7.088 \times 10^{-5}$ s $^{-1}$) were used as length and time scales, respectively. A complete list of non-dimensionalizing factors is given in Table 2. With a non-dimensional version of equations and variables, we can now introduce the new variables $\alpha = \sqrt{p_s}$, $\mu = \alpha u$, $\nu = \alpha v$, and $\tau = \alpha\sqrt{T}$, where u and v are the zonal and meridional velocity components, respectively.

Thus, total atmospheric energy (assuming hydrostatic stability) is given, in dimensionless form, by

$$E = \int_A \left(\frac{1}{2}\mu^2 + \frac{1}{2}\nu^2 + \frac{1}{\kappa}\tau^2 + \Phi_s\alpha^2 \right) dx, \quad (4)$$

where $\kappa = R/c_p$ and $R = 192$ J kg $^{-1}$ K $^{-1}$ is the gas constant per unit mass. Here, x represents the set of areographical coordinates, namely λ and ϕ representing longitude and latitude, respectively, while $\sigma = p/p_s$ acts as a terrain-following vertical coordinate. Hence, $dx = \cos\phi d\phi d\lambda d\sigma$ is a volume element in areographical coordinates. The integration is carried over the whole atmosphere. The energy scale is $E_0 = (a^2\Omega)^2 p_0/g = 89.82$ EJ (1 EJ = 10^{18} J).

Defining the state vector as $\psi = (\mu, \nu, \tau, \alpha)^T$, Eq. 4 can be identified with a squared norm

$$E = \|\psi\|^2 = (\psi, \psi). \quad (5)$$

This leads directly to the definition of the inner product as

$$(\psi^{(1)}, \psi^{(2)}) = \int_A \left(\frac{1}{2}\mu^{(1)}\mu^{(2)} + \frac{1}{2}\nu^{(1)}\nu^{(2)} + \frac{1}{\kappa}\tau^{(1)}\tau^{(2)} + \Phi_S\alpha^{(1)}\alpha^{(2)} \right) dx, \quad (6)$$

where the superindices (1) and (2) just indicate two different states and the surface pressure p_s is assumed to be time-independent.

Thus, the EOFs are the solutions to the eigenvalue equation (Berkooz *et al.*, 1993)

$$\int_A \mathbf{K}(x, x') \mathbf{E}(x') \vartheta^{(k)}(x') dx' = \Lambda^{(k)} \vartheta^{(k)}(x), \quad (7)$$

where $\Lambda^{(k)}$ and $\vartheta^{(k)}$ play the role of the k -th eigenvalue and eigenfunction, respectively. The energy matrix \mathbf{E} is the weighting function in the definition of the inner product and can be expressed as (cf. Eq. 6)

$$\mathbf{E} = \begin{pmatrix} 1/2 & 0 & 0 & 0 \\ 0 & 1/2 & 0 & 0 \\ 0 & 0 & 1/\kappa & 0 \\ 0 & 0 & 0 & \Phi_S \end{pmatrix}. \quad (8)$$

The kernel \mathbf{K} is the correlation function defined in terms of the elements of an ensemble of realizations of the system $\mathcal{S} = \{\psi^{(k)}\}_{k=1}^M$ containing M elements. Thus, \mathbf{K} is given by

$$\mathbf{K}(x, x') = \langle \psi(x) \psi^T(x') \rangle, \quad (9)$$

where $\langle \cdot \rangle$ denotes the average over \mathcal{S} . In this study, \mathcal{S} is given by the UK-MGCM dataset described in Section 2.1 and, consequently, the average over the ensemble of realizations is equivalent to a time average over the period under analysis.

The state vector can be approximated by means of the finite sum

$$\psi_N = \sum_{j=1}^N a_j \vartheta^{(j)}. \quad (10)$$

The energy contained by the approximate state vector ψ_N is, on average, (Holmes *et al.*, 1996)

$$\langle E \rangle_N = \sum_{j=1}^N \Lambda^{(j)}. \quad (11)$$

The upper index N in Eqs. 10 and 11 indicates the order of the approximation. It is possible to show that a decomposition in terms of EOFs converges more rapidly than any other linear expansion (Berkooz *et al.*, 1993; Holmes *et al.*, 1996)). This energy content is, therefore, the largest possible. The only part that remains to be determined are the coefficients a_j . By taking the inner product of $\vartheta^{(k)}$ and Eq. 10 we obtain

$$a_k = (\vartheta^{(k)}, \psi). \quad (12)$$

These time-dependent coefficients are called the principal components (PCs) of ψ and contain all the information about the evolution of the system.

Given that POD is based on variables that are products of our original variables, their interpretation becomes a little cumbersome. This disadvantage can be overcome by reconstructing the state represented by the EOFs in the following manner. EOF1 largely represent a basic atmospheric state. Thus, the reconstruction of the first mode will be based on the state given by

$$\Psi^{(1)} = \sqrt{\Lambda^{(1)}} \vartheta^{(1)}, \quad (13)$$

where $\Psi^{(1)} = (\hat{\mu}, \hat{\nu}, \hat{\tau}, \hat{\alpha})^T$. This state leads to the reconstructed fields

$$u^{(1)} = \frac{\hat{\mu}}{\hat{\alpha}} \quad v^{(1)} = \frac{\hat{\nu}}{\hat{\alpha}} \quad T^{(1)} = \frac{\hat{\tau}^2}{\hat{\alpha}^2} \quad p_s^{(1)} = \hat{\alpha}^2 \quad (14)$$

The states represented by EOFs of order $k > 1$ will be reconstructed using the state given by

$$\Psi^{(k)} = \Psi^{(1)} + \sqrt{\Lambda^{(k)}} \vartheta^{(k)}, \quad (15)$$

where $\Psi^{(k)} = (\mu^{(k)}, \nu^{(k)}, \tau^{(k)}, \alpha^{(k)})^T$. This state leads to the reconstructed fields

$$u^{(k)} = \frac{1}{\hat{\alpha}} \left(\mu^{(k)} - \frac{\hat{\mu}}{\hat{\alpha}} \alpha^{(k)} \right) \quad (16)$$

$$v^{(k)} = \frac{1}{\hat{\alpha}} \left(\nu^{(k)} - \frac{\hat{\nu}}{\hat{\alpha}} \alpha^{(k)} \right) \quad (17)$$

$$T^{(k)} = 2 \frac{\hat{\tau}}{\hat{\alpha}} \left(\tau^{(k)} - \frac{\hat{\tau}}{\hat{\alpha}} \alpha^{(k)} \right) \quad (18)$$

$$p_s^{(k)} = 2 \hat{\alpha} \alpha^{(k)} \quad (19)$$

A point that deserves further comment is concerned with the definition of TE in atmospheric dynamics. It can be argued that this definition should be based on available potential energy (APE) rather than TPE since APE is the only fraction of potential energy available to be transformed into kinetic energy (Lorenz, 1955, Lorenz, 1960). However, APE is only well-defined over isentropic or barotropic surfaces (Lorenz, 1955) which do not constitute terrain-following coordinate systems. The use of this kind of coordinate systems is desirable due to the major role that the Martian topography plays

in the dynamics of its atmosphere. The choice of TPE, on the other hand, allows the use of the terrain-following sigma-coordinates without major modifications. Nevertheless, we will see in the following sections that the thermal field splits into two parts. The first one is given by the first and most energetic EOF. This part corresponds to the background potential energy, unavailable to be transformed into kinetic energy. The second part is given by higher order EOFs. This part is comparable with APE in the sense that interactions between these EOFs correspond with exchange of APE and KE.

3.2 Short-time Fourier analysis and tidal extraction

POD and the TE norm are useful for identifying the atmospheric modes that contain most of the total energy in the atmosphere. However, these modes lack a clear physical interpretation. In an attempt to provide this interpretation, we intend to establish a relationship between the EOFs and tidal atmospheric motions. We must recall at this point that POD is not explicitly designed to extract atmospheric tides. Instead, the tidal modes should be expected to appear distributed over more than one EOF.

In order to determine the distribution of tidal modes over EOFs, it is useful to extract the tides (and other wave motions) from the raw UK-MGCM dataset. This is done by means of a new decomposition based on short-time Fourier analysis. The method is an extended version of the method outlined by Lewis and Barker (2005), which consists of a double Fourier transform in longitude and time. Unlike Lewis and Barker (2005), who only analyzed surface pressure along the equator, we performed this analysis along every

discrete latitudinal circle and height. Retaining only the frequency n and wavenumber s of interest, an inverse Fourier transform was applied to recover the tides over physical grid points.

This procedure was applied to horizontal velocity \mathbf{v} and temperature T . In order to have the three scalar components in the state vector, the tidal component of μ , ν , τ and α were then computed as

$$\mu' = \widehat{\alpha}u' + \frac{\widehat{\mu}}{\widehat{\alpha}}\alpha', \quad (20)$$

$$\nu' = \widehat{\alpha}v' + \frac{\widehat{\nu}}{\widehat{\alpha}}\alpha', \quad (21)$$

$$\tau' = \frac{\widehat{\alpha}^2}{2\widehat{T}}T' + \frac{\widehat{\tau}}{\widehat{\alpha}}\alpha', \quad (22)$$

$$\alpha' = \frac{1}{2\widehat{\alpha}}p'_s \quad (23)$$

where $(\cdot)'$ represents the tidal component of the respective variable, and $\widehat{(\cdot)}$ indicates the corresponding component in the basic state, defined as the average projection of the UK-MGCM dataset over the first and most energetic EOF given by Eq. 13.

Once tides and transient waves have been extracted, their distribution over N EOFs was computed as

$$E_k^{s,n} = \frac{1}{Z} \left\langle (a_k^{s,n})^2 \right\rangle, \quad (24)$$

where $a_k^{s,n}(t) = (\vartheta^{(k)}, \psi_{s,n}(t))$ is the projection of the wave component with frequency n and wavenumber s , denoted as $\psi_{s,n}(t)$, over the k -th EOF at

time t and

$$Z = \sum_{k=1}^N \langle (a_k^{s,n})^2 \rangle$$

is a normalization factor where N as the number of retained EOFs.

4 Eigenspectrum

To begin the POD analysis of the UK-MGCM dataset, we look at the empirical eigenspectrum based on total energy (TE). Figure 4 shows the empirical eigenvalues for the autumn-winter transition in the northern hemisphere. As expected, the first mode contains by far the majority of the atmospheric TE on average, the energy content decreasing as the EOF index increases.

The UK-MGCM eigenspectrum splits into several well-defined groups of modes of comparable energy content. Using the diagram in Fig. 4 and Fourier **Figure 4** analysis, it is possible to characterize and classify these groups according to their energy and the dominant periods present in their corresponding principal component (PC) time series. There are at least 32 groups as shown in Table 3. These include either one or two modes that share similar frequencies. We can refer to the components of these groups as singlets and doublets, respectively. A continuous tail starts with EOF41. **Table 3**

Singlets can be interpreted as non-periodic trends or standing waves. The first and second singlets (EOF1 and EOF3) carry information about the seasonal trend. When the seasonal trend is removed, the second singlet reveals the influence of the diurnal cycle. The ratios $\langle a_1^d \rangle^2 / \lambda_1 = 9 \times 10^{-8}$ and $\langle a_3^d \rangle^2 / \lambda_3 = 5 \times 10^{-2}$, where a_k^d is the projection of the diurnal tide on the k -th

EOF and λ_k is the k -th empirical eigenvalue, show the relative importance of the diurnal cycle to each of these modes. This influence is much more noticeable in PC3 than in PC1.

Doublets represent travelling waves. There are two special cases which are characterized by a single period. These are the pairs EOF2–4 and EOF9–10, characterized by a diurnal and semidiurnal period, respectively, which seem to indicate a relation between these groups and the diurnal and semidiurnal tides. Other pairs can also be characterized by their secondary period.

Figure 5 shows the normalized cumulative eddy TE (i.e. not including the EOF1) for the UK-MGCM during the period analyzed. It was normalized with respect to the average eddy TE in 1080 POD modes. The first apparent characteristic is the rapid growth in the first modes, reaching 80% with only 9 EOFs and 90% in 23 EOFs. This small number of required modes is remarkable if we compare it to the required modes to represent the terrestrial general circulation. The number of required terrestrial modes vary depending on the dataset that is taken as a basis for the POD analysis. For example, the analysis of observed geopotential height at 700 hPa for winter in the northern hemisphere in a band between 20 °N and 60 °N shows that 17 modes are required for explaining 86% variance and 36 modes explain 96% variance (Kimoto and Ghil, 1993). These numbers are certainly very comparable to the results we are presenting here for Mars. However, our study is closer in nature and method to the work by Achatz and Branstator (1999) and Achatz and Opsteegh (2003). Achatz and Branstator (1999) carried out the simultaneous analysis of global streamfunction at 200 and 700 hPa from the Community Climate Model of the National Center for Atmospheric Research

(NCAR) for perpetual January using a TE norm. They found a fairly flat spectrum and showed that as many as 500 EOFs were needed to explain 90% TE (Achatz and Branstator, 1999). This number is certainly very different even in order of magnitude to that found in the present work. Achatz and Opsteegh (2003) extended the study by Achatz and Branstator (1999) by including the seasonal cyclone and a more complete atmospheric state defined not only by streamfunction but, as in our case, by horizontal velocity and the square root of potential temperature. Interestingly enough the number of EOFs to explain 90% TE was again about 500 (Achatz and Opsteegh, 2003). This result was interpreted as an indication of the response of the terrestrial atmosphere being dependent on the same set of EOFs throughout the year. The significance of each of these relatively low-order EOFs would vary depending on the season (Achatz and Opsteegh, 2003).

Despite the different order of magnitude of the required number of EOFs to represent 90% TE on the Earth and Mars, the analysis of the Martian atmosphere by POD shows similar results as those just described for the Earth in the sense that essentially the same number of modes explain similar amount of total energy for different times of the Martian year. These modes might not be the same as those presented here. Consider for example the transient baroclinic-barotropic activity which is active during winter in each hemisphere. As we shall show in Section 5 some of the EOFs in the present analysis are closely related to this transient wave activity in the model. The analysis of a similar period for winter in the southern hemisphere would yield similar patterns in the opposite hemisphere. Assuming that we actually need around 23 EOFs to explain 90% TE in each season leads us to conjecture

that approximately 90 modes would be required throughout the Martian year. This number is still small when compared to the 500 EOFs needed in the terrestrial case.

This result suggests that the region of phase space where the UK-MGCM evolves can be represented by a few modes. This feature is due to the presence of the diurnal cycle which tends to accumulate the energy in modes largely influenced by solar heating, in particular, EOF2–4 as we shall see in the next section.

5 EOFs and atmospheric motions

In this section, we consider some of the leading EOF groups, and seek to identify them with some of the most important components of atmospheric motion. The components to be considered include atmospheric tides and transient waves.

5.1 Diurnal tide

EOF2 and EOF4 constitute the second group, sharing a similar structure and period. The corresponding principal components also share a similar behaviour, clearly showing the influence of the diurnal cycle. For example, we focus our attention first on EOF4 (Fig. 6). This is essentially a zonal wavenumber-one wave, stronger in the southern hemisphere as expected, since the original dataset corresponds to the transition from spring to summer in that hemisphere (Wilson and Hamilton, 1996). The vertical structure of EOF4 is as expected for a diurnal tide as well (cf. Wilson and Hamilton, 1996, Read

Figure 6

and Lewis, 2004). The maximum amplitude is located near the surface with a vertically propagating wavenumber-one wave above the equator. Away from the tropics, the wavenumber-one wave is vertically trapped in the lower atmosphere.

The decomposition of the diurnal tide ($n = -1 \text{ sol}^{-1}$ and $s = 1$) into a projection over the first 100 EOFs using the procedure outlined in Section 3.2 is shown in Fig. 7. As expected given the structural resemblance between EOF2–4 and the diurnal tide, the pair EOF2–4 contains 90.5% of the tidal TE whereas EOF3 contains 4.6% TE and the next most energetic group, EOF18–19, contains only 1.6%. In conclusion, the pair EOF2–4 is a good approximation to the diurnal tide in the reduced space. Alternatively, we can say that the diurnal tide is the most energetic atmospheric mode after the background state, in the dataset under analysis.

Figure 7

5.2 Semidiurnal tide

The pair EOF9–10 consists of zonal wavenumber-two waves (Fig. 8(a)). Like the semidiurnal tide, which has a vertical wavelength $> 100 \text{ km}$ (Zurek, 1981, Read and Lewis, 2004), the pair EOF9–10 also has a long vertical wavelength (Fig. 8(b)). However, the semidiurnal tide ($n = -2 \text{ sol}^{-1}$ and $s = 2$) is not quite as well represented by only one EOF pair. Performing the same decomposition analysis as for the diurnal tide case, we find that the pair EOF9–10 indeed explains 93.0% TE in the semidiurnal tide (Fig. 9). The second most energetic pair is the pair EOF33–35, which contains 1.6% TE. The third most energetic pair in the semidiurnal decomposition is the

Figure 8

Figure 9

pair EOF5–6 which explains 1.1% TE. This is still significant, especially since the pair EOF5–6 are more energetic than EOFs 9–10 when the full atmospheric motion is considered. In other words, the importance of EOF5–6 for representing the semidiurnal tide is hidden by the strong transient component in the same EOF pair.

The amplitude of the pair EOF j – k can be defined as

$$A_{j-k} = \sqrt{a_j^2 + a_k^2}, \quad (25)$$

where a_j is the j -th principal component. Plotting this diagnostic as a function of time can help to visualize the contribution of the waves to a certain motion. Thus, Figure 10 shows that indeed the contribution of EOF5–6 to the semidiurnal tide is still significant when compared to the contribution from EOF9–10. However, this signature is weak compared with the already reported maxima for EOF5–6 in their PC time series at periods of 3.6 and 3.2 sols (cf. Table 3). This case reveals the nature of the EOFs as combinations of waves that can be further separated by means of appropriate techniques. This topic will be revisited in Section 5.4 where transient baroclinic waves are analyzed by projection onto the EOF basis. EOF5–6 also contributes to the diurnal tide’s energy. However, in this case this pair is relatively unimportant to represent the diurnal tide as we have already seen in the previous section.

Figure 10

As an additional comment to the decomposition of the diurnal and semidiurnal tide, we must mention, for example, the case of pair EOF9–10 whose components appear to explain different amounts of TE in the diurnal tide

decomposition (Fig. 7). EOF9 and EOF10 are conjugated in the sense that they together can represent travelling waves of zonal wavenumber two. However, the difference in TE in the components of this pair indicates that such a wave is not a component of the diurnal tide. Therefore, these EOFs behave independently like high-order perturbations which, in this sense, are unessential for the description of the semidiurnal tide. Similarly, a zonal wavenumber-1 wave with the characteristics given by the pair EOF2–4 is not a component of the semidiurnal tide. From this point of view we can consider that POD did a remarkable job in the separation of the diurnal and semidiurnal components of the Martian thermal tides. This result is robust in the sense that this has been the case in the analysis of other times of the Martian year by these methods.

5.3 Diurnal resonant Kelvin and wavenumber-3 waves

As discussed in Section 2.1.2, the interaction between the diurnal tide and the topography, dominated by a zonal wavenumber-2 pattern, gives rise to different waves among which the diurnal resonant Kelvin and the zonal wavenumber-3 waves are the most efficiently excited. The diurnal resonant Kelvin wave is a zonal wavenumber-1 wave which propagates eastwards with period of 1 sol. The second wave that arises from the interaction of the diurnal tide with topography is a zonal wavenumber-3 mode which propagates westwards also with period of 1 sol.

The decomposition of the diurnal Kelvin wave ($n = 1 \text{ sol}^{-1}$ and $s = 1$) over 100 EOFs is shown in Fig. 11(a). This mode is distributed among several **Figure 11**

modes, most of them characterized by diurnal or nearly diurnal frequencies. The most important modes are EOF2,3,4,10 and EOF18–19. Together this set of modes explains 79% TE. The rest is distributed over various modes without clear localized energy peaks. Note that even though EOF2–4 explain a large TE in this wave, the components seem to explain a different amount of TE each. On the other hand, the diurnal wavenumber-3 wave ($n = -1 \text{ sol}^{-1}$ and $s = 3$) shows clear peaks over the pairs EOF18–19 (representing 27.6% TE) and EOF2–4 (representing 26.8% TE), already identified with westward-travelling waves with a dominant period of 1 (or nearly 1) sol (Fig. 11(b)).

5.4 Non-tidal transient waves

Generally, transient waves arise as a consequence of mixed barotropic and baroclinic instabilities and, as for the Earth, they are responsible for much of the energy transport polewards from the equator. These waves are not typically characterized by a definite wavenumber or period. Hence, the separation of these waves by means of a double Fourier transform in space and time is not as clear as in the case of tidal components. Figure 12 shows an attempt to extract projections of transient waves from the UK-MGCM dataset onto the EOFs by subtracting the tides from the complete fields. From this figure we can see that the most important contribution comes from the pairs EOF5-6 and EOF7-8, representing 45.2% and 11.5% TE, respectively. EOF1 also represents an important part of the transient activity (8.0% TE) reflecting the seasonal growth of these waves during the analyzed period.

Figure 12

EOF5–6, with a leading period of 3.6 sol and a secondary period of 3.2

sol, comprises disturbances that resemble baroclinic waves. These waves were expected since the season under analysis corresponds to an active period of baroclinic activity in the northern hemisphere (typically from late autumn to early spring in each hemisphere; Read and Lewis, 2004). Figure 13 shows contours of vertical velocity w and superimposed vectors of horizontal velocity. This figure shows that air masses moving northwards go upwards whereas air masses moving towards the equator go downwards. This structure is maintained from the surface up to an altitude of about 70 km. However, the vertical velocity field is perturbed by breaking gravity waves at altitudes above 40 km (Fig. 14). As we have seen in Section 5.2, the structure that rises to higher altitudes might also be part of the semidiurnal wave that appears as a secondary component of EOF5–6 with a period of 0.5 sols. **Figure 13**

Figure 15 shows a longitude-latitude map and a longitude-vertical section of EOF7 as representative of the pair EOF7–8. This pair consists of a wavenumber-1 travelling wave with characteristics of a baroclinic wave located around 70°N. In fact, the structure of this wave is similar to that of the pair EOF2–4. The sloping convective structure is maintained up to an altitude of 30 km whereas the thermal wave reaches heights up to 60 km at 70°N and almost 70 km at around 80°N. **Figure 14**

The amplitude evolution of each of the waves described by the EOF5–6 and EOF7–8, computed using Eq. 25, is shown in Figure 16. Also shown is the contribution of the pair EOF2–4 to the transient motion (i.e. once thermotidal motions have been removed). Unlike the diurnal and semidiurnal tides that are fairly constant (not shown here), these two transient waves exhibit large variations along the period under study. In general EOF5–6 **Figure 15**

dominates over EOF7–8 apart from the short intervals between the lines A and B and C and D where the amplitude of the latter is slightly larger than that of EOF5–6.

6 Discussion and conclusions

Through the identification of the most energetic EOFs and examining the atmospheric motions represented by them, we have achieved a clearer physical interpretation of the coherent structures represented by these EOFs. In particular, we have shown that the leading EOFs can be regarded as actual representations of those atmospheric motions known to be primary components of the general circulation on Mars, namely thermal tides and baroclinic-barotropic transient waves (e.g., Read and Lewis, 2004).

Figure 17 shows together the mean decompositions of the different kinds of motions analyzed in Section 5. The black solid line represents the eigenvalues obtained from POD. Recall that these represent the average TE represented by each EOF. The relative contribution due to the different types of wave motion can be inferred from this figure as well. The average TE explained by the first and third EOFs is, as mentioned before, due mainly to the background state, while the average TE comprised by the rest of the modes is due to either tidal motion or transient waves. The atmospheric tides that have a significant contribution towards TE are the diurnal tide (EOF2–4 and EOF18–19) and the semidiurnal tide (EOF9–10). Nevertheless, transient waves are responsible for a non-negligible amount of TE for every mode, even for those where the diurnal and semidiurnal tides play the leading role. This

Figure 17

is a clear indication of a strong relationship between thermal tides and transient baroclinic waves, a conclusion that is supported by previous studies, where the diurnal cycle has been shown to play an important role for the stability of baroclinic waves (Collins *et al.*, 1996).

On the other hand, the diurnal resonant Kelvin wave and the wavenumber-3 wave account for an amount of TE that is approximately two orders of magnitude less than the amount explained by transient waves. This result could suggest that these waves are less significant in the global context from the energy point of view at this time of the year. However, there are studies which suggest that these waves can play an important role for the development of both local and global phenomena close to the autumn equinox (Lewis and Barker, 2005, Montabone *et al.*, 2008).

Figure 17 provides an alternative tool for deciding what modes should be retained when constructing a low-order model. For instance, it shows that the diurnal pair EOF2–4 explains about the same amount of TE as the transient pair EOF5–6. A dynamical interpretation of these observations can be obtained by looking at the phase portraits described by these modes. Figure 18 shows the phase portrait of the transient component in EOF5–6 and the diurnal component in EOF2–4. This subsystem evolves over a perturbed torus and, thus, shows features of a quasiperiodic system with at least two intrinsic frequencies given by the diurnal cycle and the characteristic frequency of the transient waves. Furthermore, constructing a phase portrait with the amplitudes of the transient component in EOF5–6 and EOF7–8 and the diurnal component of PC-4 we find the characteristic two-centred phase portrait described in earlier works (Collins *et al.*, 1996; Read *et al.*, 1998).

Figure 18

This might be a further indication of a relationship between thermal tides and transient baroclinic activity. However, this would need to be confirmed, for example, by constructing a dynamical system including these modes and evaluating their actual interaction. **Figure 19**

This work is comparable, though not directly, to the work by Martínez-Alvarado *et al.* (2005). Following the analysis by Whitehouse *et al.* (2005a) on the SGCM, Martínez-Alvarado *et al.* (2005) carried out a decomposition of the same UK-MGCM dataset in vertical and horizontal modes, using the quasi-geostrophic vertical structure equation, respectively. The norm employed in POD was a TE-norm, although it was defined as the sum of KE and APE, rather than total PE, as in the present study. Despite these differences in the method, the results are similar, especially when considering the structure of the first ten modes comprising thermal tides and baroclinic waves. In Martínez-Alvarado *et al.* (2005), EOF1 and EOF2 were characterized by a diurnal period corresponding to EOF2 and EOF4 in the present study. Furthermore, their EOF2 and EOF4 mainly corresponded to transient waves as EOF5 and EOF6 do in this work. The apparent shift in order is simply due to the fact that in Martínez-Alvarado *et al.* (2005) the fields were separated into zonal (axisymmetric) and eddy parts.

So far we have shown that a dataset of atmospheric variables extracted from the UK-MGCM can be represented to a certain level of accuracy by a few leading EOFs. We have also shown that these leading EOFs represent the waves that have previously been identified as main components of the Martian general circulation. However, we know that the response of the model to solar forcing and baroclinic/barotropic instabilities are not exactly

the same as that of the actual Martian atmosphere. Therefore, the question of how these results relate to the actual behaviour of Mars' atmosphere remains open. A possible way forward is the use of the methods presented in this article to the output of data assimilation for the Martian atmosphere (Lewis *et al.*, 2007). A further hypothesis yet to be tested is whether the dynamical interaction of these few EOFs alone is able to produce a realistic evolution resembling the actual dynamics of the Martian atmosphere. We shall explore this hypothesis in a forthcoming paper.

It is appropriate here to point out that the modes are not expected to be invariant with respect to the dataset used in their derivation. Instead, a different set of EOFs is likely to be extracted from a different dataset corresponding not only to different seasons but also to the same period over different conditions, for example, under different dust loadings. The extreme case would be the study of planet-encircling dust storms which occur from time to time on Mars and are known to have an important impact over the thermal tides (Lewis and Barker, 2005). Indeed, the authors have started the analysis of this case finding that again the number of EOFs needed to give an accurate representation of the atmospheric state in terms of energy is similar to the number presented here. The patterns represented by these EOFs are altered by the sudden load of dust. This, however, is beyond the scope of the present paper.

Acknowledgements

OMA thanks the National Council for Science and Technology of Mexico (CONACYT) for the support provided to this project via the doctoral scholarship 179183.

References

- [1] Achatz, U., Branstator, G., 1999. A two-layer model with empirical linear corrections and reduced order for studies of internal climate variability. *J. Atmos. Sci.* 56, 3140–3160.
- [2] Achatz, U., Opsteegh, J.D., 2003. Primitive-equation-based low-order models with seasonal cycle. Part I: Model construction. *J. Atmos. Sci.* 60, 465–477.
- [3] Arakawa, A., Lamb, V.R., 1977. Computational design of the basic dynamical processes of the UCLA General Circulation Model. *Methods Comput. Phys.* 17, 173–265.
- [4] Barnes, J.R., 1980. Time spectral analysis of midlatitude disturbances in the Martian atmosphere. *J. Atmos. Sci.* 37, 2002–2015.
- [5] Barnes, J.R., 1981. Midlatitude disturbances in the Martian atmosphere: A second Mars year. *J. Atmos. Sci.*, 38, 225–234.
- [6] Barnes, J.R., Pollack, J.B., Haberle, R.M., Leovy, C.B., 1993. Mars atmospheric dynamics as simulated by the NASA Ames general circulation model. *J. Geophys. Res.* 98 (E2), 3125–3148.

- [7] Berkooz, G., Holmes, P., Lumley, J.L., 1993. The proper orthogonal decomposition in the analysis of turbulent flows. *Annu. Rev. Fluid Mech.* 25, 539–575.
- [8] Collins, M., James, I.N., 1995. Regular baroclinic transient waves in a simplified global circulation model of the Martian atmosphere. *J. Geophys. Res. Planet* 100 (7), 14421–14432.
- [9] Collins, M., Lewis, S.R., Read, P.L., Hourdin, F., 1996. Baroclinic wave transitions in the Martian atmosphere. *Icarus* 120, 344–357.
- [10] Forbes J.M., 2004. Tides in the middle and upper atmospheres of Mars and Venus. *Advances in Space Research* 33, 125–131.
- [11] Forget, F., Hourdin, F., Fournier, R., Hourdin, C., Talagrand, O., Collins, M., Lewis, S.R., Read, P.L., 1999. Improved general circulation models of the Martian atmosphere from the surface to above 80 km. *J. Geophys. Res. Planet* 104, 24155–24176.
- [12] Gill, A.E. 1982. *Atmosphere-ocean dynamics*. Academic Press.
- [13] Holmes, P., Lumley, J.L., Berkooz, G. 1996. *Turbulence, coherent structures, dynamical systems, and symmetry*. Cambridge Univ. Press, Cambridge, UK.
- [14] Hoskins, B.J., Simmons, A.J., 1975. A multilayer spectral model and the semi-implicit method. *Quart. J. R. Met. Soc.* 101, 637–655.
- [15] Houghton, J.T., 2002. *The Physics of Atmospheres*. Cambridge Univ. Press, Cambridge, UK.

- [16] Karhunen, K., 1946. Zur spektral Theorie stochastischer Prozesse. Ann. Acad. Sci. Fenicae A1, 34.
- [17] Lewis, S.R., Barker, P.R., 2005. Atmospheric tides in a mars general circulation model with data assimilation. *Advances in Space Research* 36, 2162–2168.
- [18] Lewis, S.R., Read, P.L., Conrath, B.J., Pearl, J.C., Smith, M.D., 2007. Assimilation of thermal emission spectrometer atmospheric data during the Mars Global Surveyor aerobraking period. *Icarus* 192, 327–347.
- [19] Loève, M. 1945. *Functions aleatoire de second ordre*. C. R. Acad. Sci. Paris.
- [20] Lorenz, E.N., 1955. Available potential energy and the maintenance of the general circulation. *Tellus* 7, 157–167.
- [21] Lorenz, E.N., 1960. Energy and numerical weather prediction. *Tellus* 12, 364–373.
- [22] Lumley, J.L. 1970. *Stochastic tools in turbulence*. Academic Press.
- [23] Martínez-Alvarado, O., Moroz, I.M., Read, P.L., Lewis, S.R. 2005. Reduced order models of the Martian atmospheric dynamics. In: *Proceedings of the 5th EUROMECH Nonlinear Dynamics Conference*. EUROMECH.
- [24] Kimoto M. and Ghil, M., 1993. Multiple flow regimes in the northern hemisphere winter. Part I. Methodology and hemispheric regimes. *J. Atmos. Sci.* 50 (16), 2625–2643.

- [25] Montabone, L., Martínez-Alvarado, O., Lewis, S.R., Read, P.L., Smith, M.D., 2007. Meteorology of the 2001 global dust storm on Mars in an assimilation of Thermal Emission Spectrometer data from Mars Global Surveyor. In: Seventh International Conference on Mars, Pasadena, California, U.S.A.
- [26] Montabone, L., Martínez-Alvarado, O., Lewis, S.R., Read, P.L., Wilson, R.J., 2008. Teleconnection in the Martian atmosphere during the 2001 planet-encircling dust storm. In: Mars atmosphere: Modeling and observations workshop, Virginia, U.S.A., abstract No. 9077.
- [27] Read, P.L., Collins, M., Früh, W.G., Lewis, S.R., Lovegrove, A.F., 1998. Wave interactions and baroclinic chaos: A paradigm for long timescale variability in planetary atmospheres. *Chaos, Solitons and Fractals* 9 (1/2), 231–249.
- [28] Read, P.L., Lewis, S.R., 2004. *The Martian climate revisited*. Springer-Praxis.
- [29] Rowley, C.W., Colonius, T., Murray, R.M., 2001. Dynamical models for control of cavity oscillations. AIAA paper 2001–2126.
- [30] Schubert, S.D., 1985. A statistical-dynamical study of empirically determined modes of atmospheric variability. *J. Atmos. Sci.* 42 (1), 3–17.
- [31] Smith, D.E., Zuber, M.T., Solomon, S.C., Phillips, R.J., Head, J.W., Garvin, J.B., Banerdt, W.B., Muhleman, D.O., Pettengill, G.H., Neumann, G.A., Lemoine, F.G., Abshire, J.B., Aharonson, O., Brown, C.D.,

- Hauck, S.A., Ivanov, A.B., McGovern, P.J., Zwally, H.J., Duxbury, T.C., 1999. The global topography of Mars and implications for surface evolution. *Science* 284, 1495–1503.
- [32] Smith, M.D., Pearl, J.C., Conrath, B.J. and Christensen, P.R., 2001. Thermal Emission Spectrometer results: Mars atmospheric thermal structure and aerosol distribution. *Journal of Geophysical Research-Planets*, 106, 23929-23945.
- [33] Smith, T.R., Moehlis, J., Holmes, P., 2005. Low-dimensional modelling of turbulence using the proper orthogonal decomposition: a tutorial. *Nonlinear Dyn.* 41, 275–307.
- [34] Whitehouse, S.G., Lewis, S.R., Moroz, I.M., Read, P.L., 2005a. A simplified model of the Martian atmosphere. Part 1: a diagnostic analysis. *Nonlinear Proc. Geophys.* 12, 603–623.
- [35] Whitehouse, S.G., Lewis, S.R., Moroz, I.M., Read, P.L., 2005b. A simplified model of the Martian atmosphere
- [36] Wilson, R.J., 1997. A general circulation model simulation of the Martian polar warming. *Geophys. Res. Lett.* 24, 123–126.
- [37] Wilson, R.J., Hamilton, K., 1996. Comprehensive model simulation of thermal tides in the Martian atmosphere. *J. Atmos. Sci.* 53, 1290–1326.
- [38] Zurek, R.W., 1976. Diurnal tide in the martian atmosphere. *J. Atmos. Sci.* 33, 321–337.

- [39] Zurek, R.W., 1981. Inference of dust opacities for the 1977 Martian great dust storms from Viking Lander 1 pressure data. *Icarus* 48, 202–215.

ACCEPTED MANUSCRIPT

Table 1: Sigma-levels and equivalent altitudes in the original dataset. The levels that were kept to perform the POD are boxed.

Level	σ	z (km)	Level	σ	z (km)
1	0.000056	97.902	14	0.455263	7.869
2	0.000250	82.940	15	0.600911	5.093
3	0.000678	72.964	16	0.731006	3.133
4	0.001542	64.747	17	0.831173	1.849
5	0.003199	57.449	18	0.899629	1.058
6	0.006290	50.688	19	0.942591	0.591
7	0.011955	44.266	20	0.968097	0.324
8	0.022181	38.085	21	0.982737	0.174
9	0.040323	32.108	22	0.990977	0.091
10	0.071666	26.357	23	0.995562	0.045
11	0.123568	20.910	24	0.998098	0.019
12	0.203945	15.899	25	0.999500	0.005
13	0.316690	11.498			

Table 2: Non-dimensionalizing factors

Dimension	Factor	Value
Length	a	3.3960×10^6 m
Time	Ω^{-1}	1.4108×10^4 s
Velocity	$a\Omega$	240.7 m/s
Temperature	$(a\Omega)^2/R$	303.1 K
Geopotential	$(a\Omega)^2$	5.794×10^4 m ² /s ²
Pressure	p_0	500 Pa
Frictional force	$a\Omega^2$	1.7062×10^{-2} m/s ²
Diabatic heat	$a^2\Omega^3/\kappa$	17.614 J(kg · s) ⁻¹

Table 3: MGCM leading EOF groups and characteristic periods. The characteristic periods are given as open intervals. The corresponding frequencies were computed with a resolution of 0.0111 sol^{-1} .

Group	Type	EOFs	Leading period (sol)	Secondary period (sol)
1	single	1	seasonal	
2	pair	2, 4	diurnal	
3	single	3	seasonal	weak diurnal
4	pair	5, 6	(3.52, 3.67)	(3.15, 3.27)
5	pair	7, 8	(4.38, 4.61)	(3.99, 4.18)
6	pair	9, 10	semidiurnal	
7	single	11	seasonal	
8	single	12	(1.711, 1.744)	(1.619, 1.648)
9	single	13	(35.9, 59.9)	(1.711, 1.744)
10	single	14	seasonal	(1.619, 1.648)
11	single	15	seasonal	
12	single	16	(35.9, 59.9)	(1.619, 1.648)
13	single	17	(25.7, 59.9)	
14	pair	18, 19	(1.004, 1.015)	(0.982, 0.993)
15	single	20	(35.9, 59.9)	(3.67, 3.82)
16	single	21	seasonal	(25.7, 35.9)
17	pair	22, 23	(1.779, 1.815)	(1.679, 1.711)
18	single	24	(25.7, 35.9)	(2.85, 2.94)
19	single	25	(1.372, 1.393)	(1.116, 1.130)
20	single	26	(1.116, 1.130)	(35.9, 59.9)
21	single	27	(35.9, 59.9)	19.9, 25.7)
22	single	28	(3.99, 4.18)	(2.95, 3.05)
23	single	29	(25.7, 35.9)	(3.67, 3.82)
24	single	30	(2.76, 2.85)	(1.744, 1, 779)
25	single	31	(1.852, 1.891)	(1.116, 1.130)
26	single	32	(3.15, 3.27)	(6.20, 6.65)
27	pair	33, 35	(0.501, 0.503)	(0.495, 0.498)
28	pair	34, 36	(0.332, 0.333)	(0.501, 0.503)
29	pair	37, 39	(0.501, 0.503)	(0.332, 0.333)
30	single	38	(0.332, 0.333)	(19.97, 25.7)
31	single	40	(19.97, 25.7)	(1.744, 1, 779)
32	continuous	≥ 41	various	various

Figure captions

Figure 1: Temporal and zonal average of temperature (gray scale), zonal wind (white) and meridional mass transport streamfunction (black) in the UK-MGCM dataset. Solid, dashed and dotted lines represent positive, negative and null contours, respectively. The separation between contours is $\Delta u = 27.0 \text{ m s}^{-1}$ for zonal velocity, and $\Delta \chi = 129.2 \text{ kg s}^{-3}$ for mass streamfunction.

Figure 2: Planetary waves in the UK-MGCM dataset as seen in (a) surface pressure, and (b) temperature at $\sigma = 0.943$ (approximate height $z = 600\text{m}$ above the planetary surface). Both figures correspond to an equatorial longitude circle. Negative periods indicates westward travelling waves.

Figure 3: Planetary waves in the UK-MGCM dataset as seen in (a) surface pressure, and (b) temperature at $\sigma = 0.943$ (approximate height $z = 600\text{m}$ above the planetary surface). Both figures correspond to a longitude circle at 64.3°N . Negative periods indicates westward travelling waves.

Figure 4: Eigenvalues obtained from POD of the UK Mars GCM.

Figure 5: Cumulative energy in the UK Mars GCM normalized with respect to the total energy in 1080 EOFs (without considering energy in the first EOF).

Figure 6: Temperature in EOF4 (in K): (a) Longitude-latitude map at

$\sigma = 0.8$ ($z \simeq 1.8$ km above the planetary surface) (gray contours represent topography); (b) latitude-altitude section at 150°E , and longitude-altitude sections (c) at the equator and (d) 35°S .

Figure 7: Mean diurnal tide decomposition over 100 EOFs (showing only the first 60).

Figure 8: Temperature, in K, in the EOF9: (a) Longitude-latitude map at $\sigma = 0.8$ ($z \simeq 1.8$ km above the planetary surface) (gray contours represent topography); (b) longitude-altitude section at 18°N .

Figure 9: Mean semidiurnal tide decomposition over 100 EOFs (showing only the first 60).

Figure 10: Amplitude evolution (defined in text) of the pairs EOF9-10 and EOF5-6 in the semidiurnal tide decomposition.

Figure 11: Mean distribution over 100 EOFs (showing only the first 60) of (a) the diurnal Kelvin wave and (b) westward propagating diurnal wavenumber-3 wave.

Figure 12: Mean distribution of transient waves over 100 EOFs (showing only the first 60).

Figure 13: MGCM EOF5 vertical velocity (in m s^{-1}) contours on a northern hemisphere longitude-latitude map at $z \simeq 32$ km. The arrows represent horizontal velocity.

Figure 14: Longitude-altitude sections at 64.3°N showing (a) vertical velocity (in m s^{-1}) and (b) temperature (in K) in EOF5.

Figure 15: (a) Longitude-latitude map at $z \simeq 32$ km, and (b) longitude-altitude section at 70.2°N of temperature (in K) in EOF7.

Figure 16: Amplitude evolution of the pairs EOF5–6 and EOF7–8 in the transient wave decomposition. Also included is amplitude evolution of the transient component in the pair EOF2–4.

Figure 17: Mean distribution of tidal and non-tidal atmospheric motions over 40 EOFs.

Figure 18: Phase portrait of the transient component in EOF5–6 and the diurnal component in EOF4.

Figure 19: Phase portrait of the transient component amplitude in the pairs EOF5–6 and EOF7–8 and the diurnal component in PC-4. The two centres of evolution are labelled with the letters A and B.

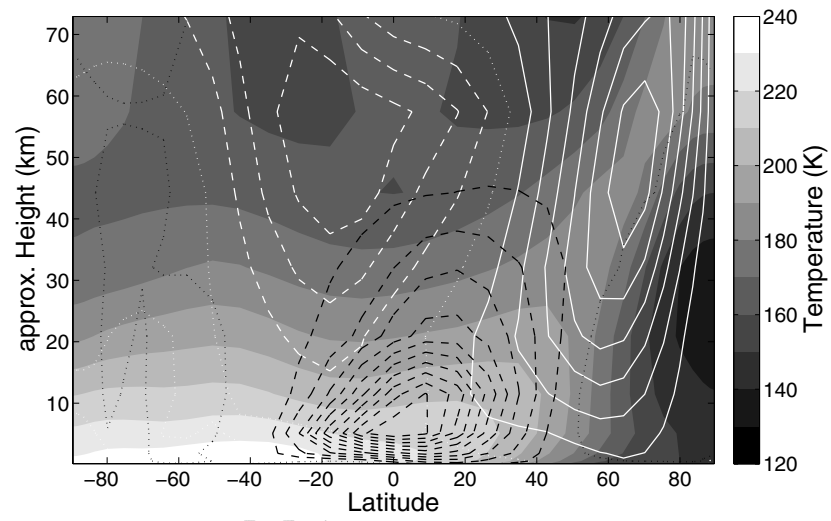
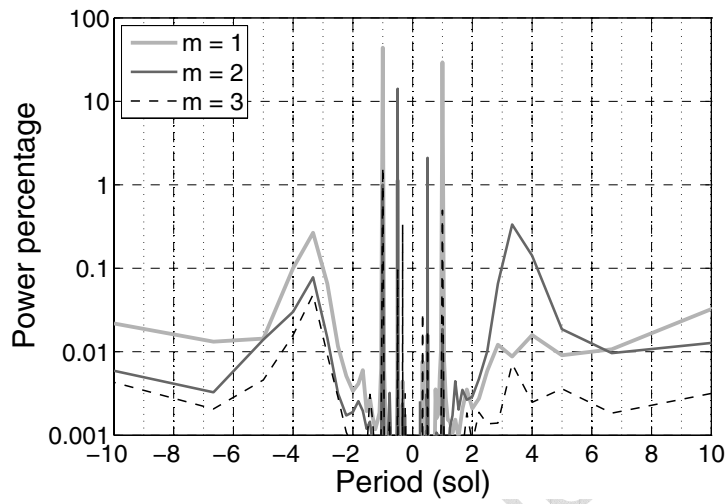
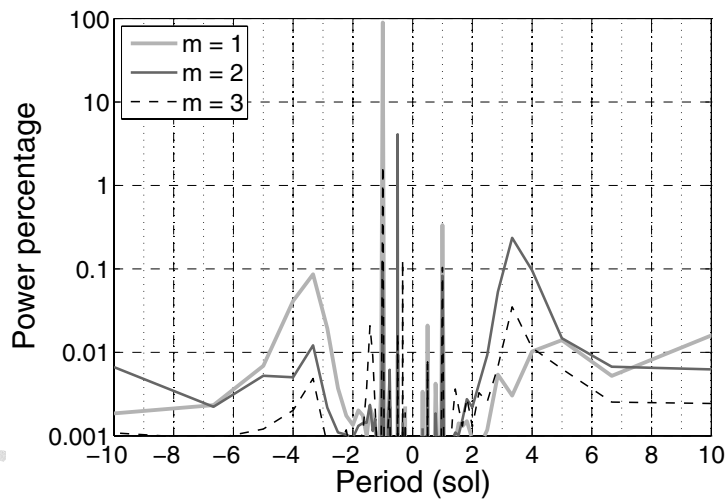


Figure 1: O. Martínez-Alvarado, I. M. Moroz, P. L. Read, S. R. Lewis and L. Montabone.

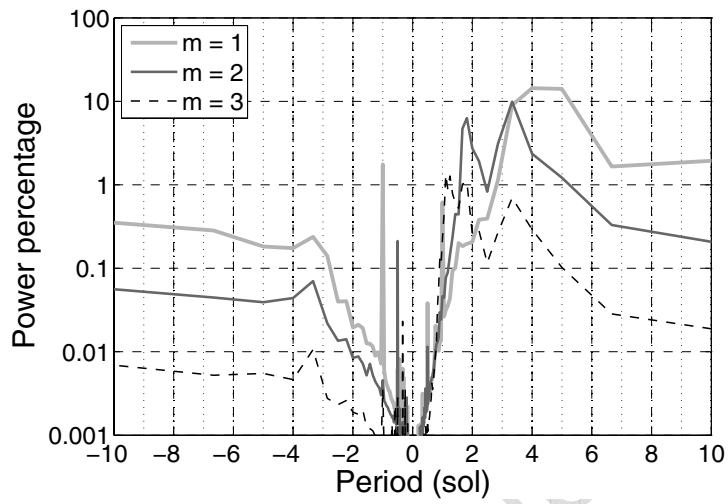


(a)

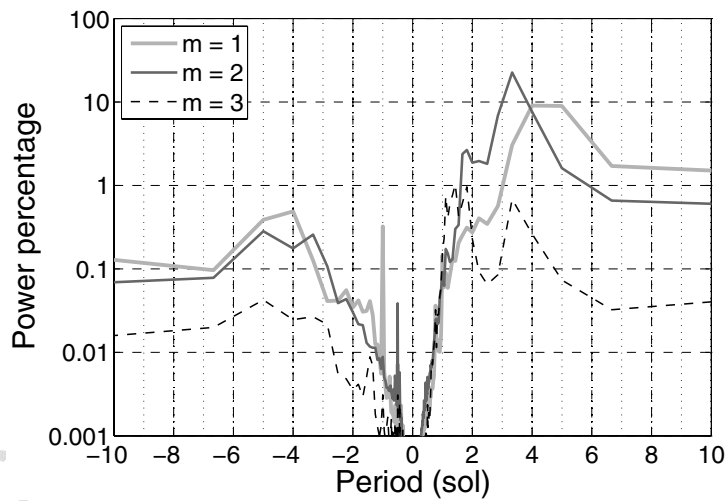


(b)

Figure 2: O. Martínez-Alvarado, I. M. Moroz, P. L. Read, S. R. Lewis and L. Montabone.



(a)



(b)

Figure 3: O. Martínez-Alvarado, I. M. Moroz, P. L. Read, S. R. Lewis and L. Montabone.

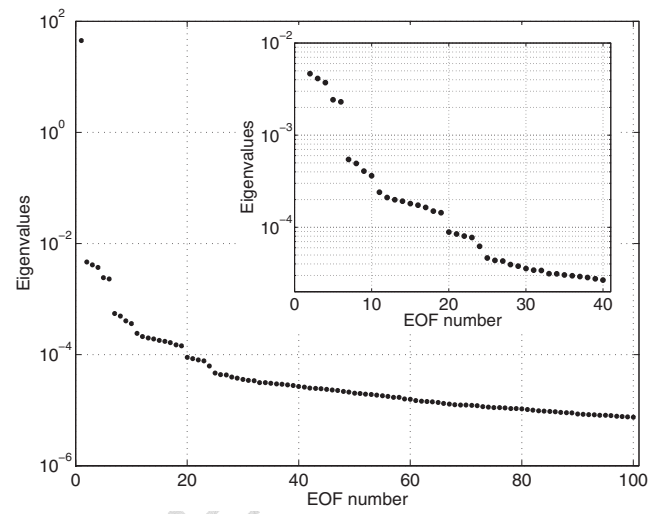


Figure 4: O. Martínez-Alvarado, I. M. Moroz, P. L. Read, S. R. Lewis and L. Montabone.

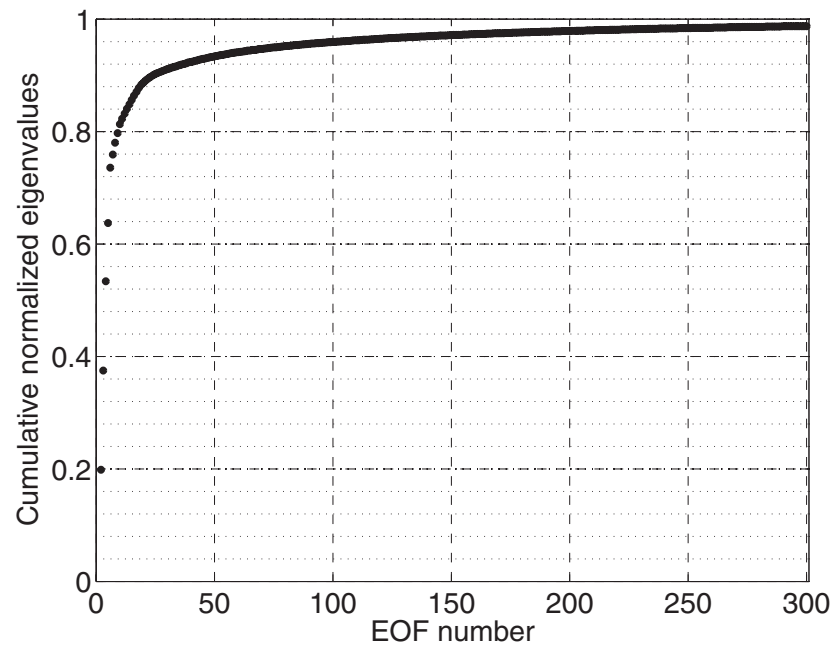


Figure 5: O. Martínez-Alvarado, I. M. Moroz, P. L. Read, S. R. Lewis and L. Montabone.

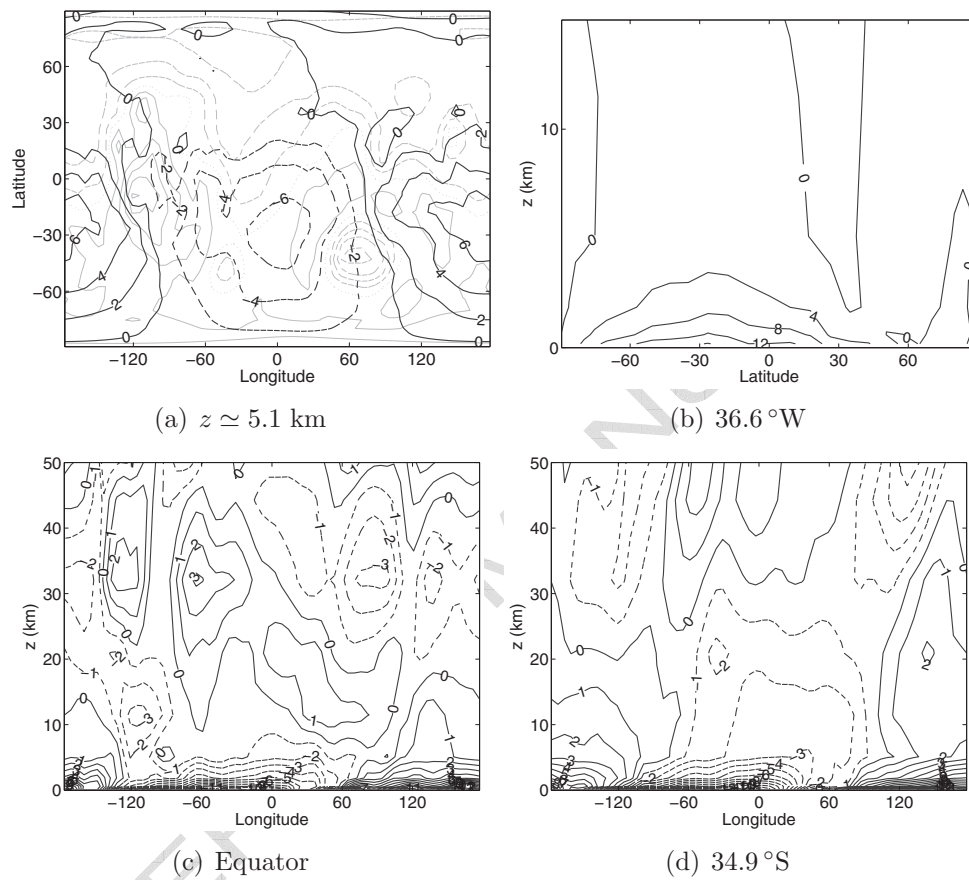


Figure 6: O. Martínez-Alvarado, I. M. Moroz, P. L. Read, S. R. Lewis and L. Montabone.

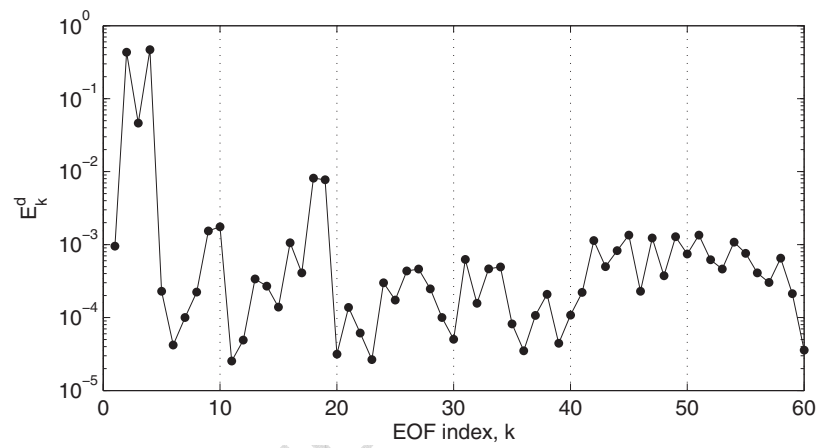


Figure 7: O. Martínez-Alvarado, I. M. Moroz, P. L. Read, S. R. Lewis and L. Montabone.

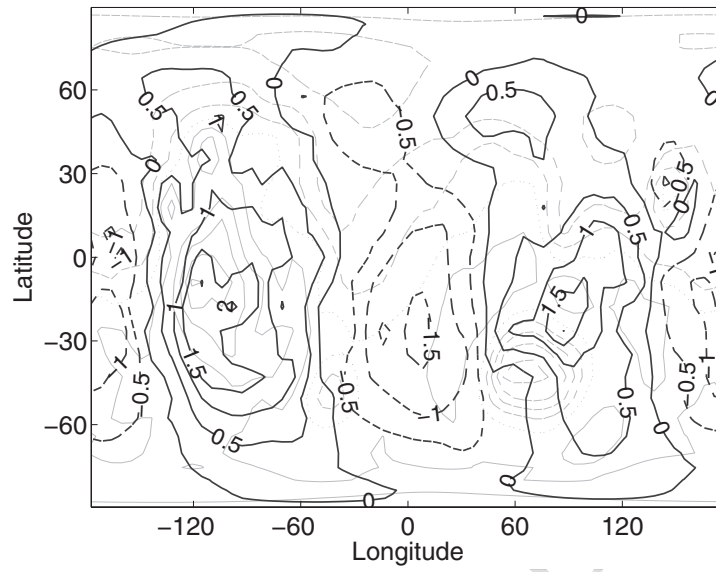
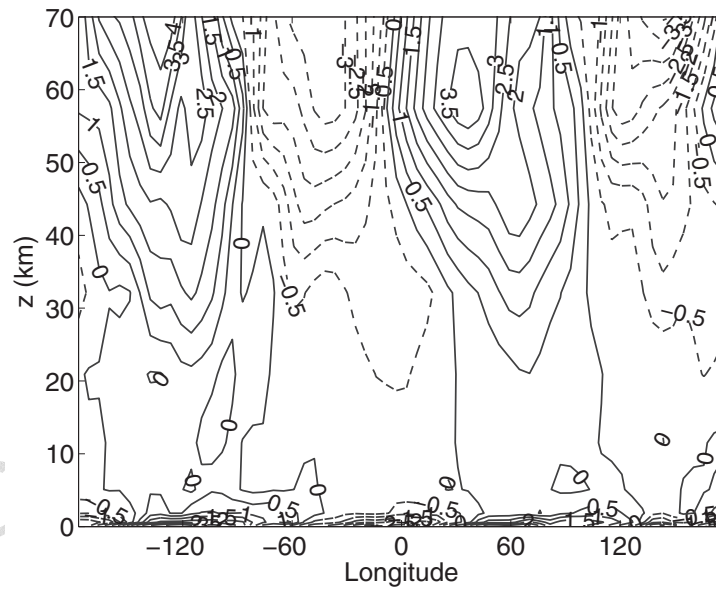
(a) $z \approx 174$ m(b) 17.8° N

Figure 8: O. Martínez-Alvarado, I. M. Moroz, P. L. Read, S. R. Lewis and L. Montabone.

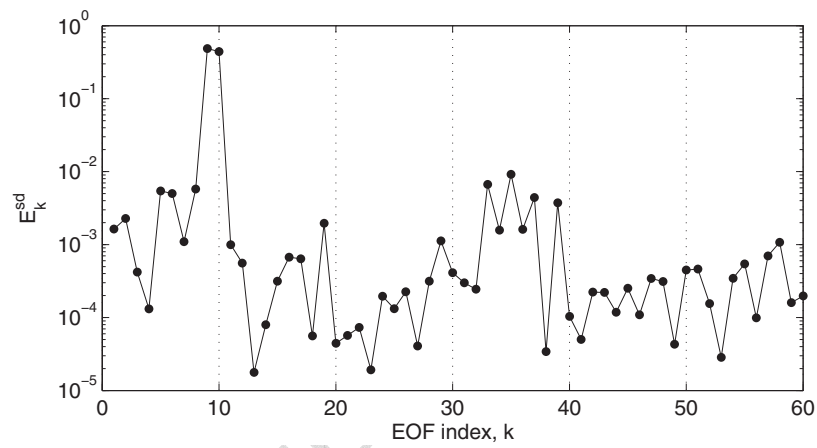


Figure 9: O. Martínez-Alvarado, I. M. Moroz, P. L. Read, S. R. Lewis and L. Montabone.

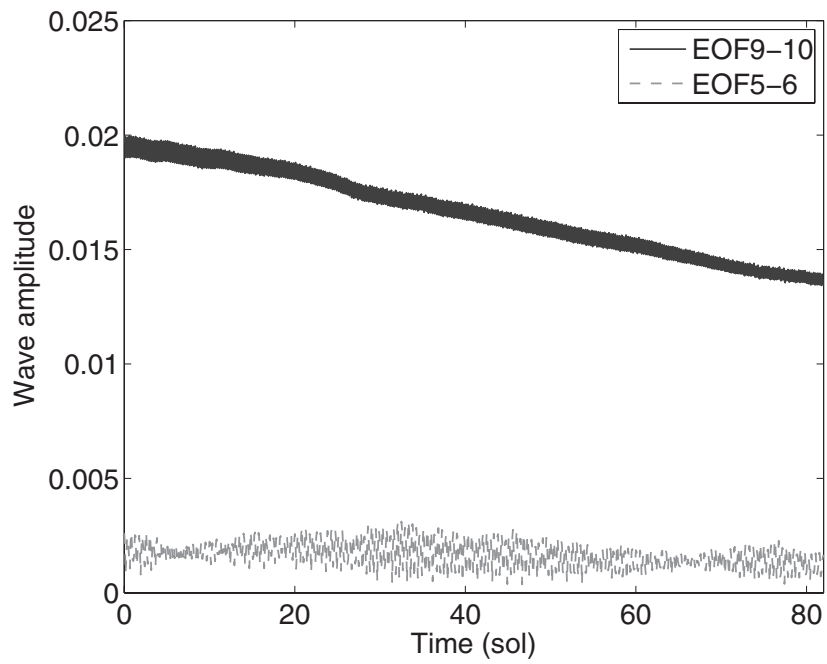
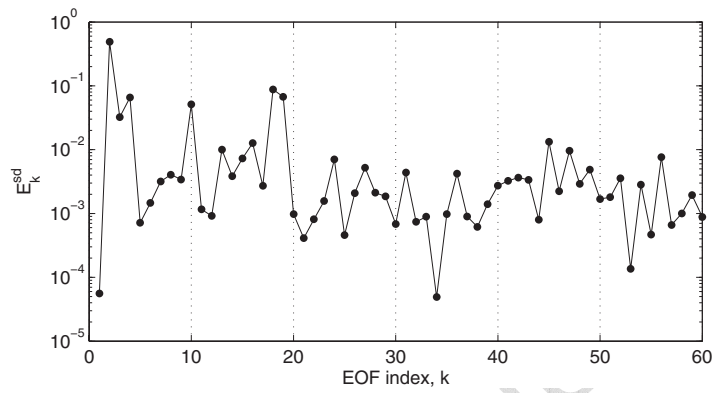
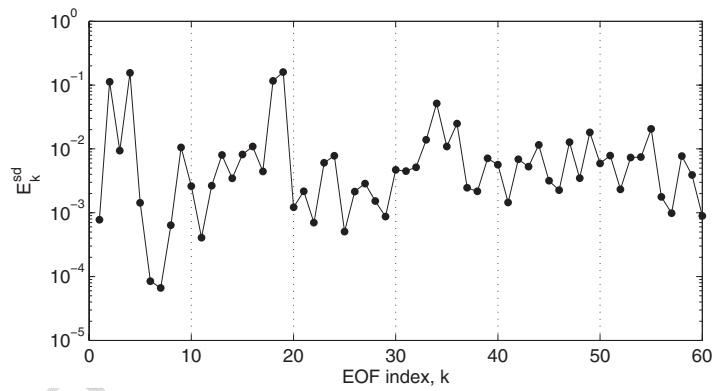


Figure 10: O. Martínez-Alvarado, I. M. Moroz, P. L. Read, S. R. Lewis and L. Montabone.



(a) Diurnal Kelvin wave



(b) Diurnal wavenumber-3 wave

Figure 11: O. Martínez-Alvarado, I. M. Moroz, P. L. Read, S. R. Lewis and L. Montabone.

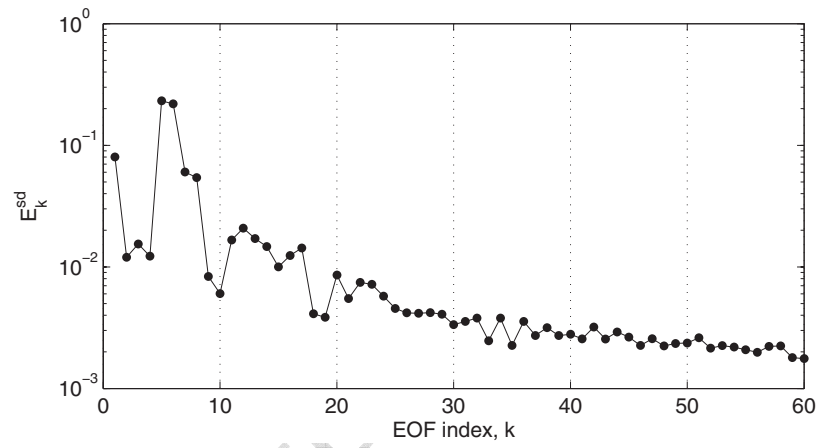


Figure 12: O. Martínez-Alvarado, I. M. Moroz, P. L. Read, S. R. Lewis and L. Montabone.

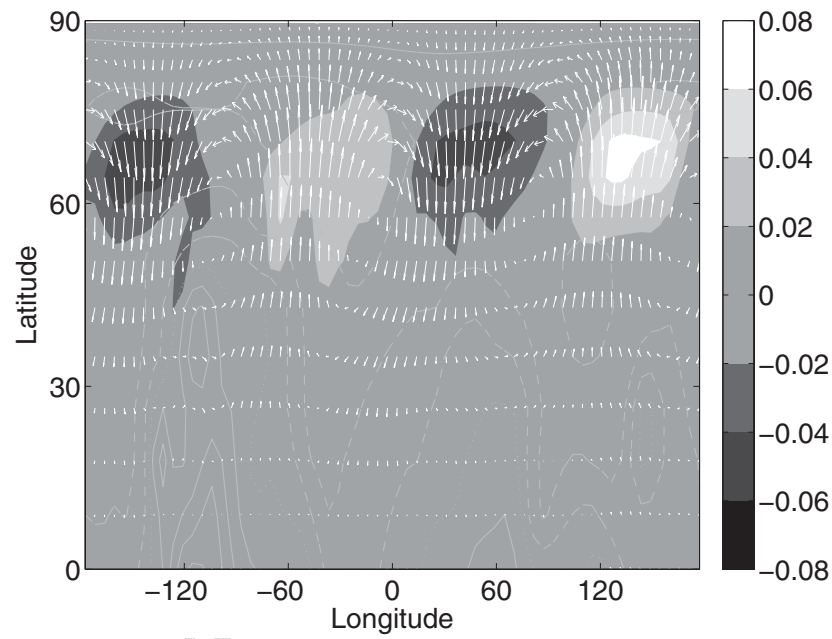


Figure 13: O. Martínez-Alvarado, I. M. Moroz, P. L. Read, S. R. Lewis and L. Montabone.

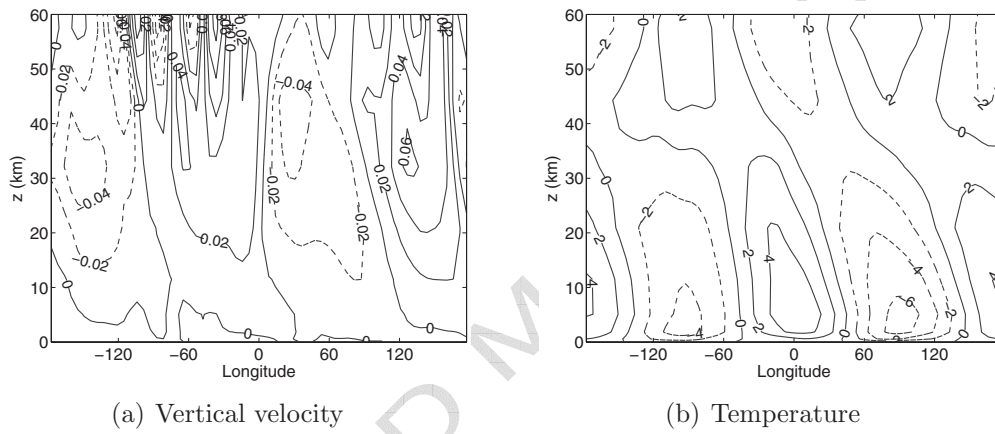


Figure 14: O. Martínez-Alvarado, I. M. Moroz, P. L. Read, S. R. Lewis and L. Montabone.

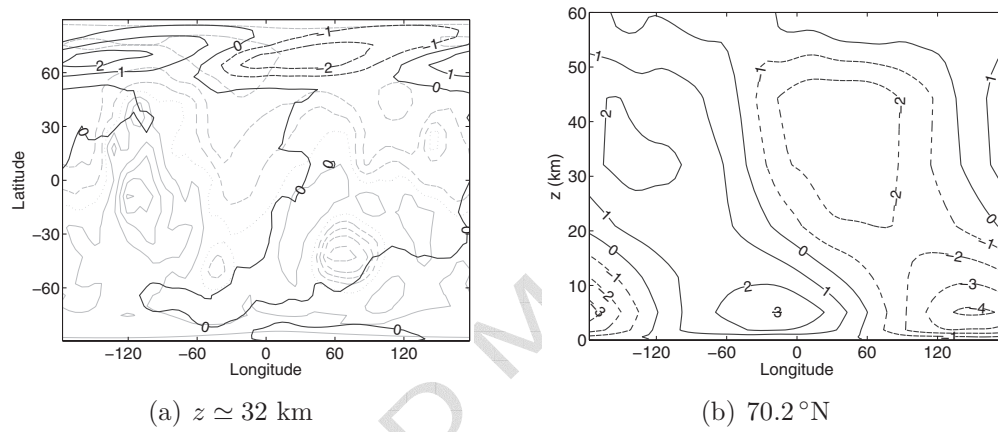


Figure 15: O. Martínez-Alvarado, I. M. Moroz, P. L. Read, S. R. Lewis and L. Montabone.

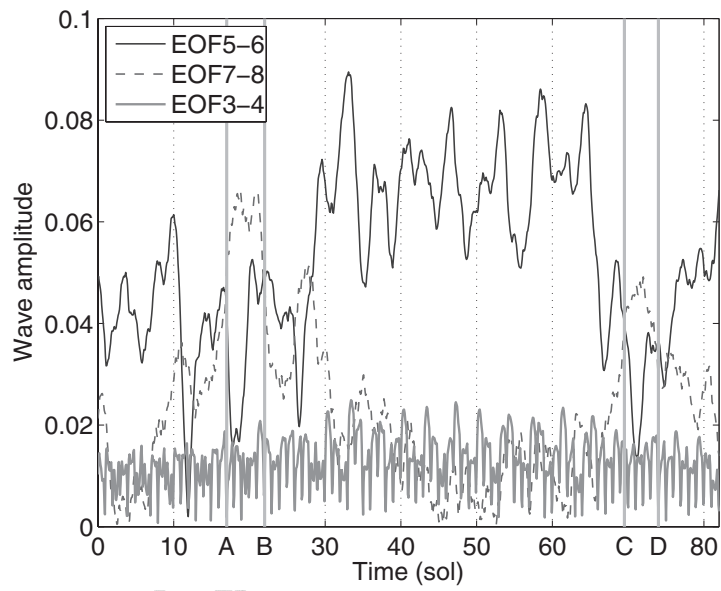


Figure 16: O. Martínez-Alvarado, I. M. Moroz, P. L. Read, S. R. Lewis and L. Montabone.

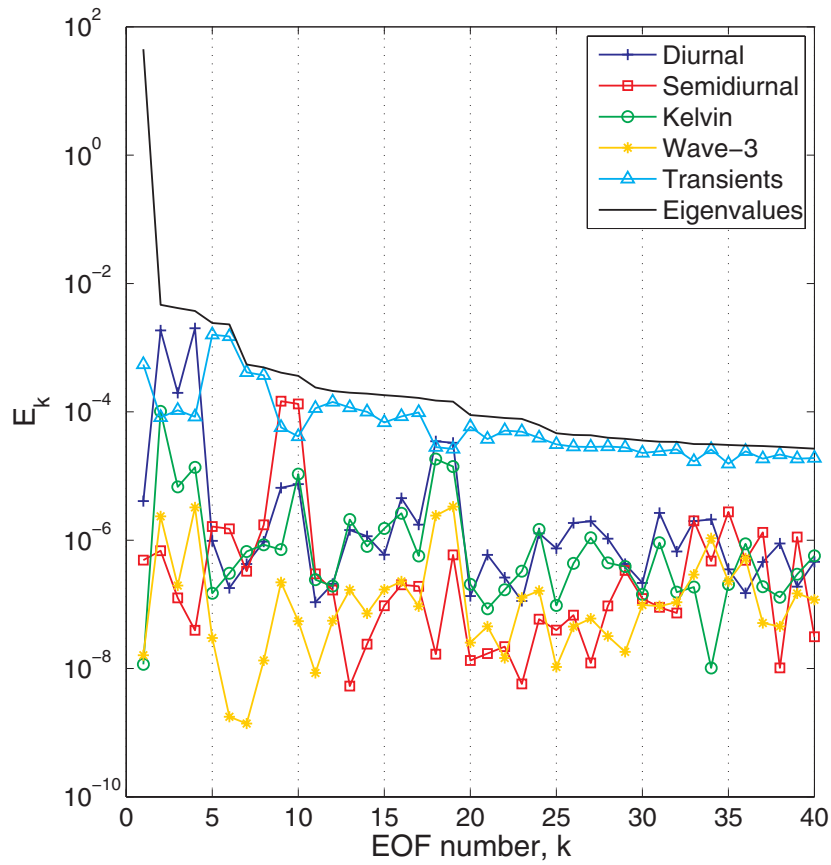


Figure 17: O. Martínez-Alvarado, I. M. Moroz, P. L. Read, S. R. Lewis and L. Montabone.

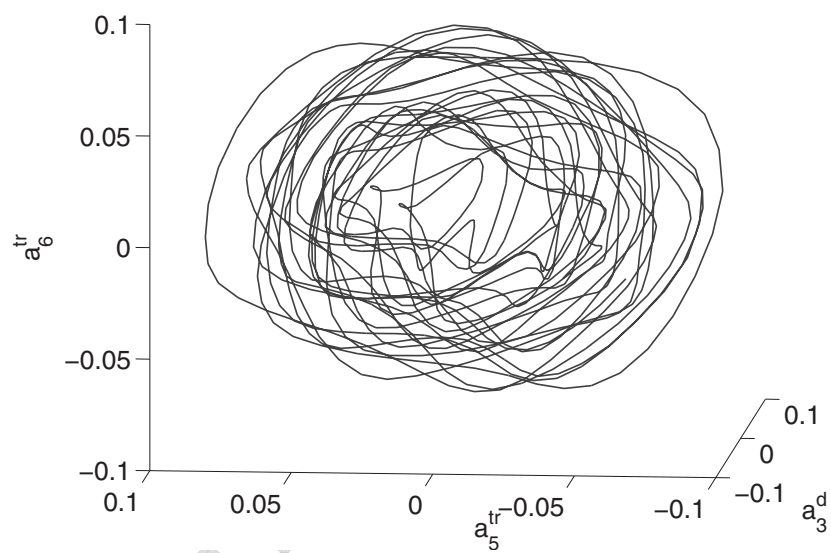


Figure 18: O. Martínez-Alvarado, I. M. Moroz, P. L. Read, S. R. Lewis and L. Montabone.

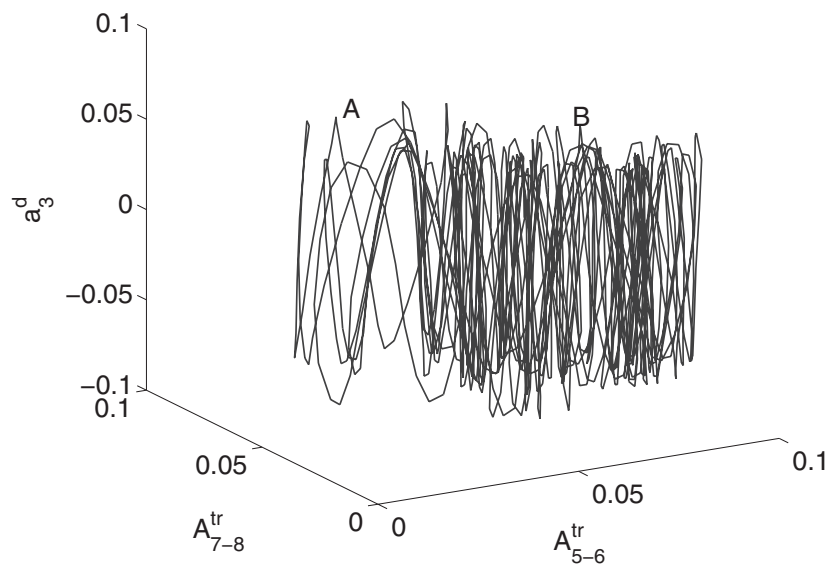


Figure 19: O. Martínez-Alvarado, I. M. Moroz, P. L. Read, S. R. Lewis and L. Montabone.